JOTCS A
Journal of the Turkish Chemical Society
Section: A
Chemistry
TURKISH CHEMICAL SOCIETY

Effect of Nd^{3+} Doping on Structural, Near-Infrared, and Cathodoluminescent Properties for Cadmium Tantalate Phosphors

Lütfiye Feray Güleryüz*

*Department of Mechanical Engineering, Ege University, Bornova, 35040, İzmir, Turkey

Abstract: $Cd_{1-x}Ta_2O_6$:xNd^{3+} (x=0.5, 1.5, 3, 5, 7, and 10 mol%) phosphor series were fabricated by conventional solid state method at 1100 °C for 17 hours. The samples of cadmium tantalate were investigated by structural (XRD, SEM) and spectroscopic (CL, PL) analyses. In XRD results, the symmetry of $CdTa_2O_6$ phase with orthorhombic columbite structure was confirmed between 0.5 and 10 mol% Nd^{3+} doping concentrations. SEM analysis of the grains revealed round and shapeless morphology while grain sizes ranged from submicron to several microns. The emission spectra of $Cd_{1-x}Ta_2O_6$:xNd^{3+} (x=0.5, 1.5, 3, 5, 7 and 10 mol%) phosphor series recorded with the transitions of $^4F_{3/2}\rightarrow{}^4I_{9/2}$ and $^4F_{3/2}\rightarrow{}^4I_{11/2}$. Among these transitions, the transition $^4F_{3/2}\rightarrow{}^4I_{9/2}$ (at 889 nm) has a high near-infrared emission intensity, which can be attributed to the laser potential of the phosphor. The NIR emission of the phosphor increased with increasing concentration of Nd^{3+} up to 5 mol% and then declined because of concentration quenching phenomenon. The CL emission peak at about 450 nm found in all samples is related to the intrinsic emission of the cadmium tantalate host. In addition, Nd^{3+} doped phosphors exhibited the $^4F_{3/2}\rightarrow{}^4I_{9/2}$ transition of Nd^{3+} and defect-related CL emissions at 670 nm. Decreasing crystallinity with increasing Nd^{3+} concentration caused a decrease in host emission intensity at 450 nm.

Keywords: $CdTa_2O_6$; Cathodoluminescence; Nd^{3+}; Near infrared luminescence.

Submitted: November 10, 2022. Accepted: December 29, 2022.

Cite this: Güleryüz LF. Effect of Nd^{3+} Doping on Structural, Near-Infrared, and Cathodoluminescent Properties for Cadmium Tantalate Phosphors. JOTCSA. 2023;10(1):77–88.

DOI: https://doi.org/10.18596/jotcsa.1202284.

***Corresponding author. E-mail:** ferayguleryuz@hotmail.com

INTRODUCTION

The phosphors, which are doped with the rare-earth (RE) ions, have some convenient features such as remarkable efficiency, long lifetime, energy saving, enhanced physical robustness, kindly to environment properties, smaller size and faster switching (1-22). Among RE^{3+} (trivalent) ions, Nd (neodymium) is one of the earliest RE^{3+} ions used in solid-state lasers. Therefore, Nd^{3+} activated materials are well-known as solid-state phosphors due to their laser emissions at beneficial wavelengths such as $^4F_{3/2}\rightarrow{}^4I_{9/2}$ transition and also the other possible transitions $^4F_{3/2}\rightarrow{}^4I_{15/2}$, $^4F_{3/2}\rightarrow{}^4I_{13/2}$ and $^4F_{3/2}\rightarrow{}^4I_{11/2}$ (15-22). Among the $^4F_{3/2}\rightarrow{}^4I_J$ transitions of Nd^{3+} ion, the $^4F_{3/2}\rightarrow{}^4I_{9/2}$ transition at 880 nm finds application as a powerful diode laser transition. The $^4F_{3/2}\rightarrow{}^4I_{11/2}$ transition stands out due to its ability to be easily operated at room temperature and pumped efficiently by flash lamp. The lasing transition at 1350 nm ($^4F_{3/2}\rightarrow{}^4I_{13/2}$) is finding application as tele-communication transition window (22). The cathodoluminescence (CL) produced in the UV-visible-NIR system of the electromagnetic

spectrum is due to the interaction of the material with the electron beam, where optical characterization is performed by means of the cathode rays (fast electrons) provided by an electron gun and the luminescence (light emission) formed. The CL analysis can be interpreted via spectral lines that are similar to those from other luminescence techniques, and characteristically dominate the spectrum with bound excitonic states and changes from emission lines, donor-acceptor double bands, and defect-related properties (23–27).

The ternary oxides of general formula AB_2O_6 ($A=M^{2+}$, $B=Nb^{5+}$, Ta^{5+}) crystallize in the columbite structure. The cations of A and B are located in the center of the octahedra surrounded by six oxygen atoms while the AO_6 and BO_6 octahedra share the edges, forming independent zigzag chains. This sequential situation repeats as ABBABB octahedral layers as the chains are connected by sharing corners in order to the AO_6 chain-BO_6 chain-BO_6 chain (5-11). $CdTa_2O_6$, as an AB_2O_6 oxide structure, has been studied in the literature in terms of its luminescence and thermodynamic properties. The white-light properties of Dy^{3+} doped $CdTa_2O_6$, and the PL-RL properties of Eu^{3+} doped $CdTa_2O_6$ have been reported by (7) and, (8) respectively. The molar heat capacity of $CdTa_2O_6$ has been reported as 179.65 J mol^{-1} K^{-1}, at ambient temperature (28). In addition, cadmium-containing phosphor materials are attracting attention in the field of optics as a new material class due to their broad potential applications such as solar cells, biosensors, biomedical scanning, and light-emitting diodes (LEDs) (29-33). The inherent toxicity of cadmium limits its applications, especially in the industrial and biomedical fields, so the genotoxicity and cytotoxicity of CdSe/ZnS (cadmium selenide/Zinc sulfide) core/shell QDs for applications in cancer therapy have been discussed (34). However, cadmium-based phosphors provide a high level of brightness, leading to a reduction in the need for high levels of X-ray doses, which can minimize the risk of health problems (29,35).

In the study, NIR photoluminescence and cathodoluminescence of $Cd_{1-x}Ta_2O_6:xNd^{3+}$ (x=0.5, 1.5, 3, 5, 7, 10 mol%) phosphors were studied. The spectroscopic and structural characterizations of the samples were carried out by XRD, SEM-EDS, FTIR, PL, and CL analyses.

EXPERIMENTAL SECTION

Undoped and $Cd_{1-x}Ta_2O_6:xNd^{3+}$ ($0.005\leq x\leq 0.1$ or $0.5\leq x\leq 10$ mol%) materials were fabricated using solid state reaction. Nd_2O_3 (Alfa Aesar, 99.9%) was used as a dopant. $Cd(NO_3)_2.4H_2O$ (Sigma-Aldrich, 99%) and Ta_2O_5 (Alfa Aesar, 99.9%) powders were used as starting materials. The powders of $Cd(NO_3)_2.4H_2O$, Ta_2O_5 and Nd_2O_3 were prepared and homogenized in agate mortar according to stoichiometry of $Cd_{1-x}Ta_2O_6:xNd^{3+}$ where $CdTa_2O_6$ (x=0), $Cd_{0.995}Nd_{0.005}Ta_2O_6$ (x=0.005), $Cd_{0.985}Nd_{0.015}Ta_2O_6$ (x=0.015), $Cd_{0.97}Nd_{0.03}Ta_2O_6$ (x=0.03), $Cd_{0.95}Nd_{0.05}Ta_2O_6$ (x=0.05), $Cd_{0.93}Nd_{0.07}Ta_2O_6$ (x=0.07), $Cd_{0.90}Nd_{0.10}Ta_2O_6$ (x=0.1), respectively. Prepared powders were sintered at 1100 °C for 17 hours in an electric furnace under air atmosphere after pelleting.

The phase structure of the ceramics were performed by X-ray diffraction (D-MAX 2200, Rigaku Corp., Japan) using Cu-K_α radiation, Ni filter, scan rate = 2 °/min, and 2θ=20-65°. The grain morphology and elemental identification of the ceramic samples were carried out by SEM (JSM-5910LV, JEOL Ltd., Japan) equipped with EDS (INCAx-Sight 7274, Oxford Industries, UK) after Au/Pd (gold/palladium) coating. FTIR (fourier transform infrared spectrometer) spectra were taken by Perkin–Elmer ATR–FTIR. Near emission spectra of powders were measured in the range of 850-1450 nm using a diode laser of 800 nm excitation at 300 K. Cathodoluminescence (CL) spectra were performed with a monochromatic spectrometer (DATAN-Mono CL4) attached to an electron microscope (NOVA-NANOSEM 650) with an emission gun (working distance 6.6 mm, voltage 15 kV, spot size 3.5) in high vacuum. Besides CL imaging, the spectrometer allows acquisition of CL spectra at highly localized points of a sample.

RESULTS AND DISCUSSION

Structural and Morphological Characterization

Figure 1 shows the XRD results of undoped sample and $Cd_{1-x}Ta_2O_6:xNd^{3+}$ (x=0.5, 1.5, 3, 5, 7 and 10 mol%) samples. The XRD patterns of the samples (JCPDS card No.39-1431) can be indexed space group *Pbcn*. As seen in the XRD patterns of all the samples, there are no different minor phases in the range of two theta degree (for 20° and 65°). The cell parameters of $CdTa_2O_6$ structure are a=5.8510 Å, b=14.7847 Å, c=5.1462 Å, and V=445.17 $Å^3$ (36). The orthorhombic structure of $CdTa_2O_6$ along the c-

axis has been illustrated in Figure 2. Octahedra with the same central cation share edges forming zigzag chains along the c-axis while TaO_6 octahedra of adjacent chains share corners to form double layers, parallel to the *bc*-plane, which are connected via CdO_6 octahedra through common corners (37). On the basis of the ion radius and coordination number (CN), the formation of the single-phase can be attributed to the substitution of Nd^{3+} ions with ionic radius 0.983 Å (for 6 C.N) by Cd^{2+} ions (r=0.95 Å, for C.N. 6). Figure 3 shows the XRD peaks of the (131) reflection. As seen in the XRD peaks, there was a slight shift towards smaller two theta angles due to the increase in Nd^{3+} concentration. This may be attributed to the expansion of the lattice volume due to the slightly large ionic radius of the Nd^{3+} ion, where the Nd^{3+} substitution instead of Cd^{2+} is also likely to affect the charge balance and form some stress in the structure, albeit limited. However, despite some expansion in the lattice volume, the existence of the single-phase structure was preserved up to 10 mol% concentration, indicating that the dopant ion has located into the structure successfully.

SEM micrographs at 10.000x magnification of undoped and 0.5, 3, and 10 mol% Nd^{3+} doped samples are shown in Figure 4(a-d). The grain shapes of Nd^{3+} doped samples have elliptical shapes and a shapeless morphology, while the grain sizes varied from 0.5 to 3.5 µm. Figure 5 shows the EDS spectra and elemental compositions of (weight%, atomic%) and theoretical atomic (%) values for $Cd_{1-x}Ta_2O_6$:Nd^{3+} grains were detected by EDS at 20 kV of SEM acceleration voltage, where atomic (%) compositions are compatible with theoretical atomic (%) values.

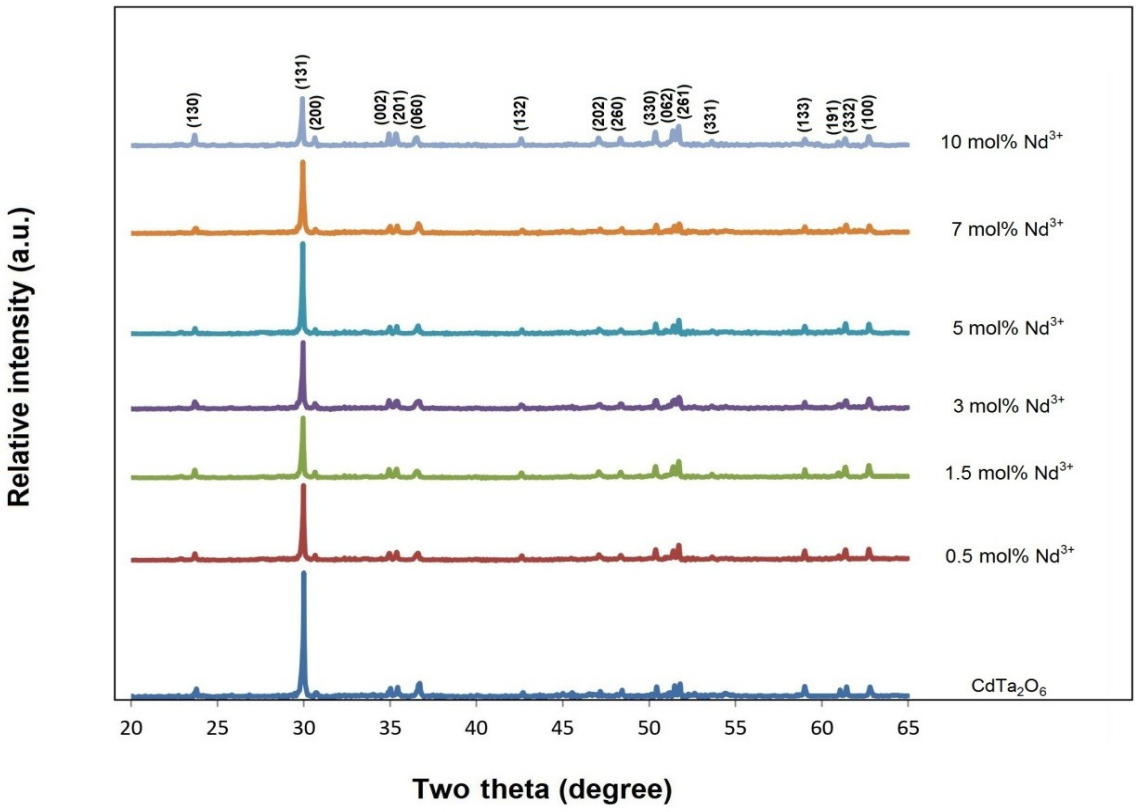

Figure 1: XRD results of undoped and $Cd_{1-x}Ta_2O_6$:xNd^{3+} (x=0.5, 1.5, 3, 5, 7, and 10 mol%) samples.

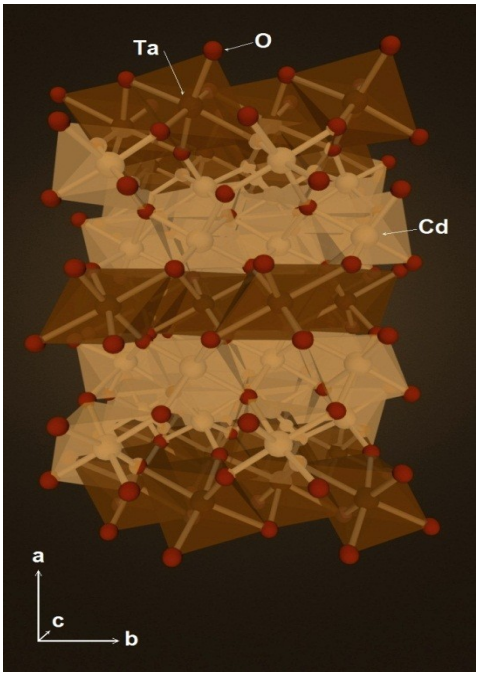

Figure 2: Schematic illustration of the $CdTa_2O_6$ crystal in the direction of the c axis.

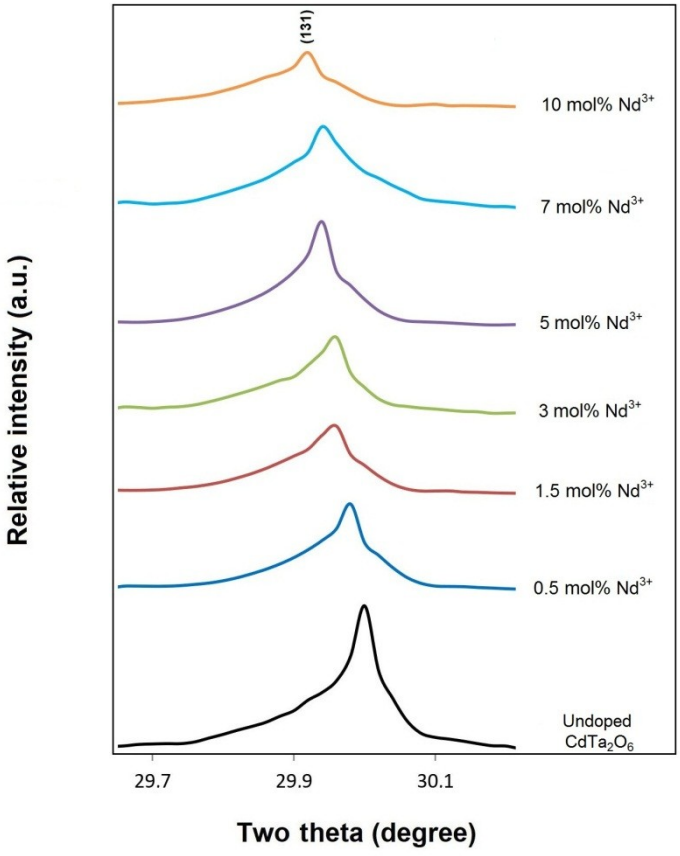

Figure 3: XRD two theta angles (131) shifted to lower angles with Nd^{3+} concentration.

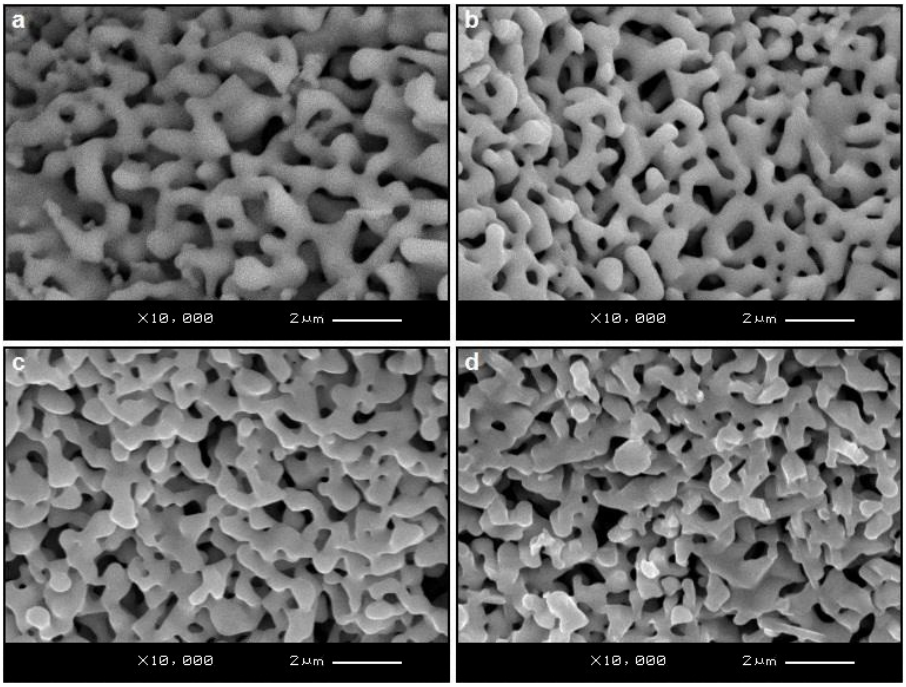

Figure 4: SEM micrographs of (a) undoped and (b) 0.5, (c) 3, (d) 10 mol% Nd^{3+} doped samples at 20 kV acceleration voltage, and 10.000× magnification.

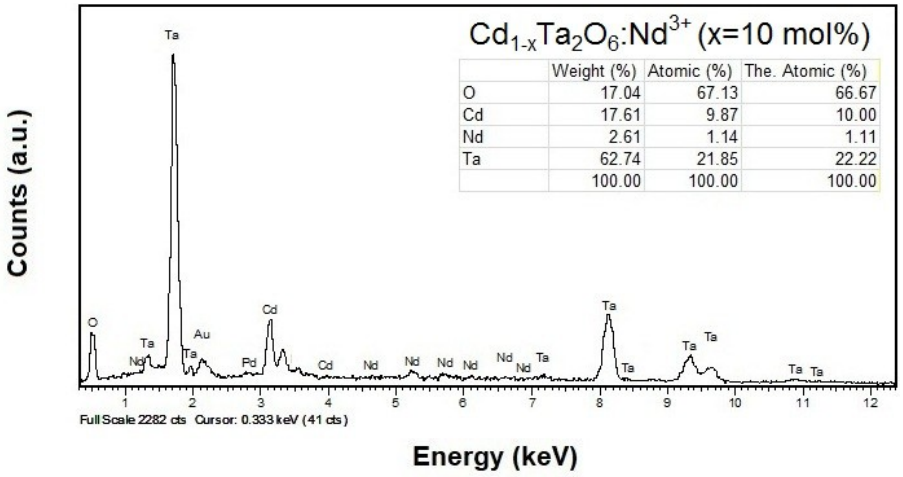

Figure 5: EDS spectrum and compositions (wt%, at%) and theoretical at% values for 10 mol% Nd^{3+} doped sample.

FTIR Analysis

FTIR spectra of undoped sample and $Cd_{1-x}Ta_2O_6$:xNd^{3+} (x=1.5, 5 and 10 mol%) samples in the range of 500–4000 cm^{-1} are presented in Figure 6. The molecular structure of the metal oxides with IR spectroscopy can be detected from M=O vibrations in the 500–1000 cm^{-1} while the peaks of 2800-4000 cm^{-1} shows the fundamental stretching of OH groups (38). FTIR peaks of 800-1000 cm^{-1} can be associated with the Ta–O bond vibrations while the small peaks in between 1000-1500 cm^{-1} are due to Cd–O–Ta vibrations.

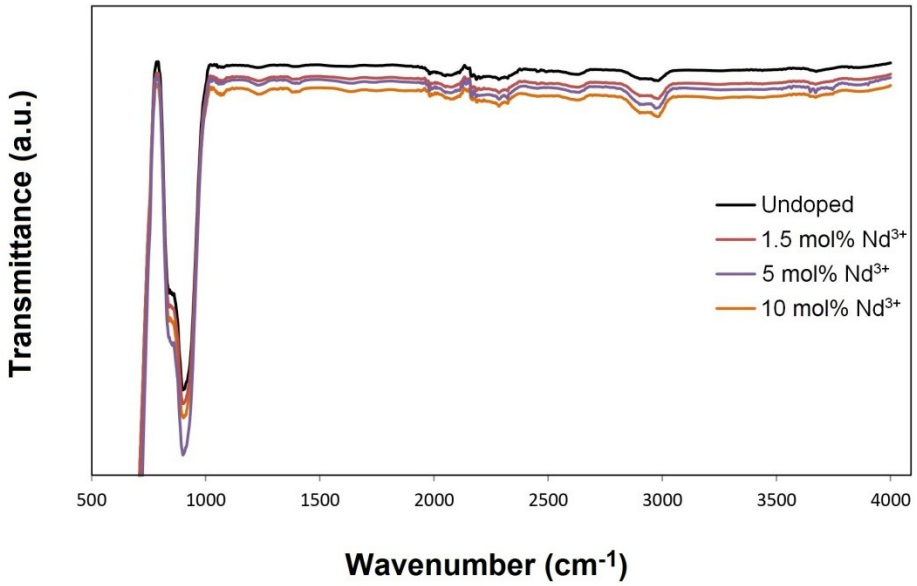

Figure 6: FTIR spectra of undoped and $Cd_{1-x}Ta_2O_6$:xNd^{3+} (x=1.5, 5, 10 mol%) samples.

NIR luminescence of $Cd_{1-x}Ta_2O_6$:xNd^{3+} (x=0.5, 1.5, 3, 5, 7 and 10 mol%) phosphors

Figure 7 shows the NIR emission spectra of $Cd_{1-x}Ta_2O_6$:xNd^{3+} (x=0.5, 1.5, 3, 5, 7, 10 mol%) phosphors were used a laser diode with excitation source 800 nm. The emissions of the phosphors were monitored corresponding to the $^4F_{3/2}\rightarrow{}^4I_{9/2}$ and $^4F_{3/2}\rightarrow{}^4I_{11/2}$ transitions at 889 and 1073, respectively. The $^4F_{3/2}\rightarrow{}^4I_{9/2}$ transition (at 889 nm) is a potential laser transition that appears to be more intense than the $^4F_{3/2}\rightarrow{}^4I_{11/2}$. Although the overall energy level of the 4f electrons of the Nd^{3+} ion protected by the outer shell $5s^2$ and $5p^6$ electrons does not vary greatly in different hosts, the energy level surrounding the Nd^{3+} ions can be subdivided into 2J+1 sublevels by the local crystal field (39). As seen in Figure 7, there are many splits resulting from the $^4F_{3/2}\rightarrow{}^4I_{9/2}$ transition with the highest emission peak in the 860–940 nm range, while the $^4F_{3/2}\rightarrow{}^4I_{11/2}$ transition exhibits emission around 1070 nm. The Stark components of both transitions of Nd^{3+} ions are similar, which can be associated with the similarity of local symmetry of ligand ions surrounding the Nd^{3+} ion (19-21). The near infrared emission of the phosphor rose up to 5 mol%, and emission declined at 7 and 10 mol% concentrations. The decrease in PL density may be associated with higher Nd^{3+} concentrations (or beyond 5% mol), which promotes the migration of excitation energy between active ions (22,40). As Nd^{3+} concentration continues to increase, cross-relaxation mechanism between Nd^{3+}-Nd^{3+} ions becomes more and more important, and therefore non-radiation transitions will be more likely to occur due to the nearness between the Nd^{3+} ions (17).

Cathodoluminescence of undoped and Cd1-xTa2O6:xNd3+ (x=1.5, 5, and 10 mol %) phosphors

Figure 8 shows the cathodoluminescence spectra of undoped sample and $Cd_{1-x}Ta_2O_6$:xNd^{3+} (x=1.5, 5, and 10 mol%) phosphors. In CL emissions, the peak at about 450 nm is related to the intrinsic emission of the polycrystal host, and is present in all samples (41,42). For the similar compound, orthorhombic columbite $CdNb_2O_6$, the host emission has been reported as 460 nm (43,44). Accordingly, the CL host emission of $CdTa_2O_6$ observed at 450 nm is consistent with the PL host emission of $CdNb_2O_6$. On the other hand, the undoped sample has the highest host emission intensity, while the intrinsic emission intensity of Nd^{3+} doped samples at 450 nm decreases with increasing concentration. This is due to the inclusion of Nd^{3+} ion in the lattice affected the crystallinity (45). As seen from the CL spectra, 10 mol% Nd^{3+} doped phosphor has lowest intrinsic emission intensity, which can be attributed to the fact that Nd^{3+} doping causes the most distortion (or the highest effect on crystallization) at this concentration. The emission peak of Nd^{3+} doped phosphors at about 670 nm (red emission) show a red

emission which is associated with the defect related to deep emission (45,46), the recombination of electrons in the non-bridging oxygen band-gap state with holes in the valence band edge (47,48). The final luminescence peak of 900 nm indicates neodymium emission from the 4f shell transition of Nd^{3+} ions corresponding to the ground state ($_4I^{9/2}$) from the excited state ($_4F^{3/2}$) in the host lattice (49).

CL micrographs of undoped sample and $Cd_{1-x}Ta_2O_6$:xNd^{3+} (x=1.5, 5, 10 mol%) phosphors are shown in Figure 9(a-d). In CL micrographs, the undoped sample has a blue emission appearance due to the 450 nm peak (as mentioned earlier), while the doped samples show blue-red-blue emissions due to the 450 and 670 nm peaks.

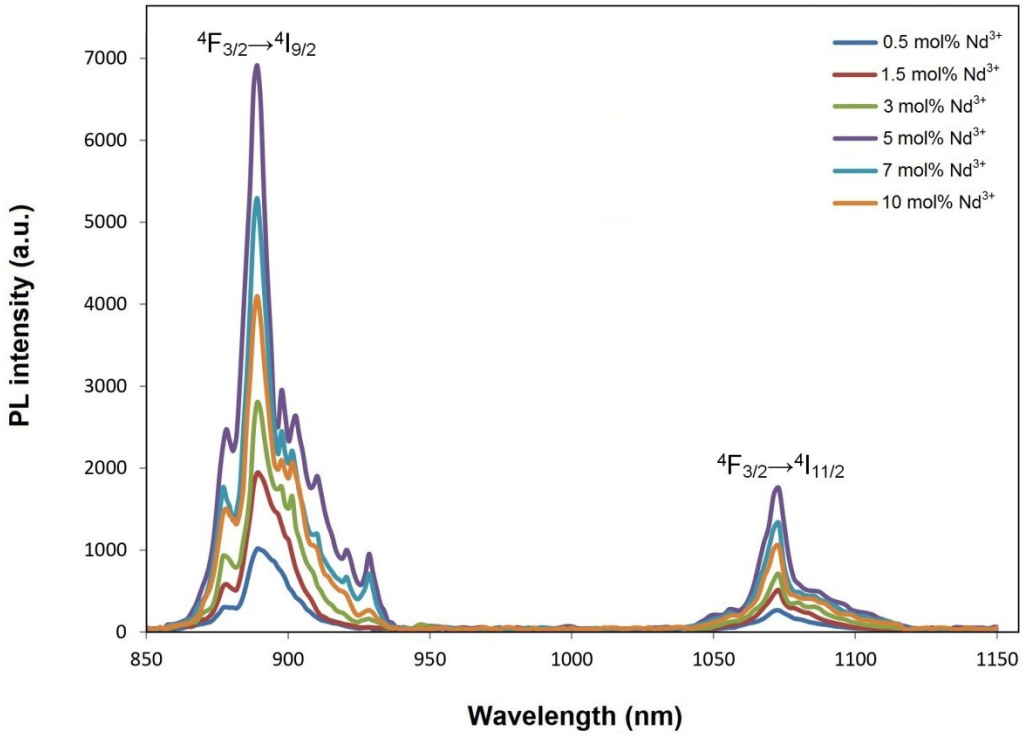

Figure 7: Near-infrared emission spectra of $Cd_{1-x}Ta_2O_6$:xNd^{3+} (x=0.5, 1.5, 3, 5, 7, and 10 mol%) phosphors by diode laser under 800 nm excitation.

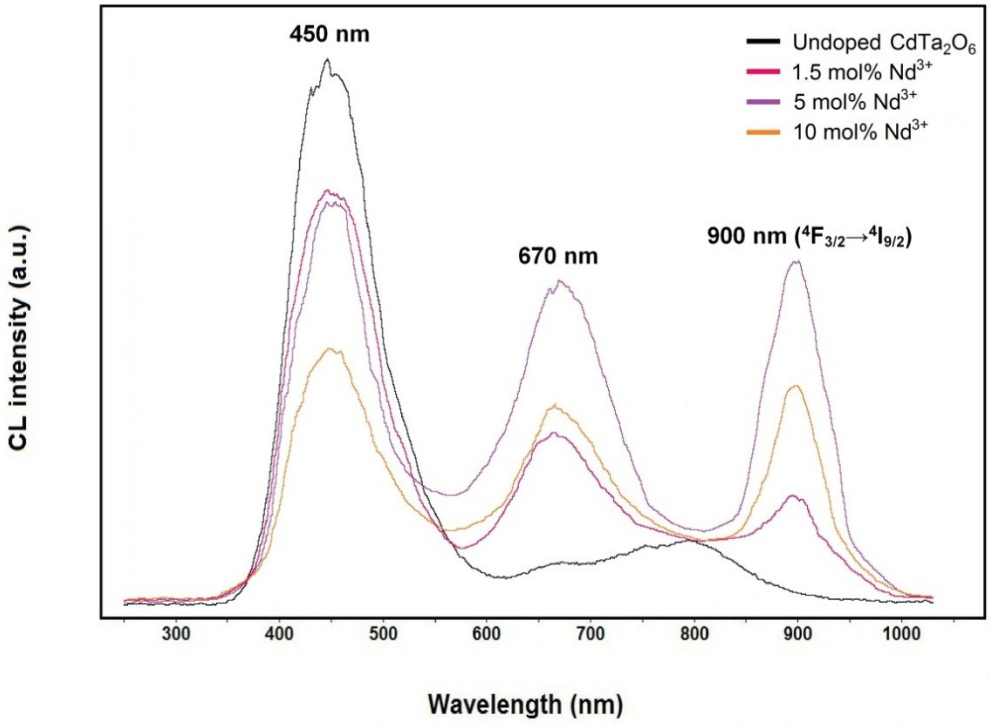

Figure 8: CL emission spectra of undoped $CdTa_2O_6$, and $Cd_{1-x}Ta_2O_6$:xNd^{3+} (x=1.5, 5, and 10 mol%) phosphors.

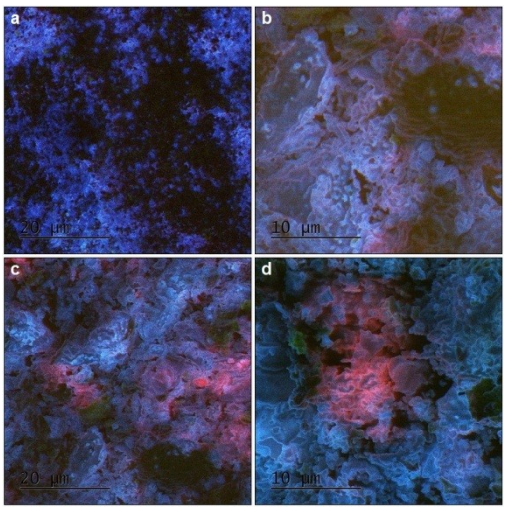

Figure 9: CL micrographs for (a) undoped sample, and (b) 1.5, (c) 5, (d) 10 mol% Nd^{3+} doped cadmium tantalate phosphors.

CONCLUSION

$Cd_{1-x}Ta_2O_6$:xNd^{3+} (x=0.5, 1.5, 3, 5, 7 and 10 mol %) phosphors were fabricated by solid state method. XRD results indicated the presence of the single phase Nd^{3+} concentrations from 0.5 to 10 mol%. SEM examinations revealed the shapeless/rounded grain morphology with the sizes of 0.5-3.5 micron while EDS identified elemental compositions of the grains. The NIR

emissions of the phosphors monitored with the transitions of $^4F_{3/2}\rightarrow{}^4I_{9/2}$ (889 nm) and $^4F_{3/2}\rightarrow{}^4I_{11/2}$ (1073 nm), where the $^4F_{3/2}\rightarrow{}^4I_{9/2}$ transition is a potential laser transition that appears to be more intense than the $^4F_{3/2}\rightarrow{}^4I_{11/2}$. The CL emission of undoped sample was observed with the peak of 450 nm, in which the decreased CL intensity of the phosphors is related to the effect of crystallinity. Nd^{3+}-doped phosphors exhibited the 900 nm peak due to the $^4F_{3/2}\rightarrow{}^4I_{9/2}$ transition, as well as the 450 and 670 nm peaks of structural origin. Based on the observed results, it could be concluded that the $Cd_{1-x}Ta_2O_6:Nd^{3+}$ phosphor with the strong transition of $^4F_{3/2}\rightarrow{}^4I_{9/2}$ has potential for diode lasing applications.

CONFLICT OF INTEREST

There is no conflict of interest.

REFERENCES

1. Ekmekçi MK. Influence of europium doping on the crystallization, morphology, and cathodoluminescent properties of $PbNb_2O_6:Eu^{3+}$ phosphors. JOTCSA. 2022;1129–1140. <URL>.

2. Nagaraj R, Rajagopal V, Raja A, Ranjith S. Influence of Dy^{3+} ion concentration on photoluminescence and energy transfer mechanism of promising KBaScSi3O9 phosphors for warm white LEDs. Spectrochim. Acta A Mol. Biomol. Spectrosc. 2022;264:120212. <URL>.

3. İlhan M, Katı Mİ, Keskin İÇ, Güleryüz LF. Evaluation of structural and spectroscopic results of tetragonal tungsten bronze $MTa_2O_6:Eu^{3+}$ (M = Sr, Ba, Pb) phosphors and comparison on the basis of Judd-Ofelt parameters. J. Alloy. Comp. 2022;901:163626. <URL>.

4. Yao S, Lv S, Feng Z. Synthesis and photoluminescent properties of Dy^{3+}:$CaYAlO_4$ phosphors. Appl. Phys. A 2021;127:773. <URL>.

5. Ekmekçi MK, İlhan M, Güleryüz LF, Mergen A. Study on molten salt synthesis, microstructural determination and white light emitting properties of $CoNb_2O_6:Dy^{3+}$ phosphor. Optik. 2017 Oct;128:26–33. <URL>.

6. İlhan M, Ekmekçi MK, Keskin İÇ. Judd–Ofelt parameters and X-ray irradiation results of $MNb_2O_6:Eu^{3+}$ (M = Sr, Cd, Ni) phosphors synthesized via a molten salt method. RSC Adv. 2021 Feb;11:10451. <URL>.

7. İlhan M, Ekmekçi MK. Synthesis and photoluminescence properties of Dy^{3+} doped white light emitting $CdTa_2O_6$ phosphors. J. Solid State Chem. 2015;226:243–249. <URL>.

8. İlhan M, Keskin İÇ Photoluminescence, radioluminescence and thermoluminescence properties of Eu^{3+} doped cadmium tantalate phosphor. Dalton Trans. 2018;47:13939-13948. <URL> .

9. Erdem R, İlhan M, Ekmekçi MK, Erdem Ö. Electrospinning, preparation and photoluminescence properties of $CoNb_2O_6:Dy^{3+}$ incorporated polyamide 6 composite fibers. Appl. Surf. Sci. 2017;421:240-246. <URL>.

10. Başak AS, Ekmekçi MK, Erdem M, İlhan M, Mergen A. Investigation of boron-doping effect on photoluminescence properties of $CdNb_2O_6:Eu^{3+}$ phosphors. J. Fluoresc 2016;26:719–724. <URL>.

11. İlhan M, Keskin İÇ. Analysis of Judd–Ofelt parameters and radioluminescence results of $SrNb_2O_6:Dy^{3+}$ phosphors synthesized via molten salt method. Phys. Chem. Chem. Phys. 2020;2:19769. <URL>.

12. He X, Fang B, Zhang S, Lu X, Ding J. Preparation and properties of Nd-doped BCTH lead-free ceramics by solid-phase twin crystal method. Curr. Appl. Phys. 2022;38;30–39. <URL>.

13. İlhan M, Güleryüz LF, Keskin İÇ, Katı Mİ. A comparison of spectroscopic properties of Dy^{3+}-doped tetragonal tungsten bronze MTa_2O_6 (M = Sr, Ba, Pb) phosphors based on Judd–Ofelt parameters. Mater. Sci: Mater. Electron 2022;33:16606–16620. <URL>.

14. İlhan M, Keskin İÇ. Evaluation of structural behaviour, radioluminescence, Judd-Ofelt analysis and thermoluminescence kinetic parameters of Eu^{3+} doped TTB–type lead metaniobate phosphor. Phys. B: Condens. Matter 2020;585:412106. <URL>.

15. He X, Fang B, Zhang S, Lu X, Ding J. Preparation of nanoscale $[(Ba_{0.85}Ca_{0.15})_{0.995}Nd_{0.005}](Ti_{0.9}Hf_{0.1})O_3$ ceramics via hydrothermal method and effect of grain size on multifunctional performance. J. Alloys Compd. 2022;925:166249. <URL>.

16. İlhan M, Keskin İÇ, Çatalgöl Z, Samur R. NIR photoluminescence and radioluminescence characteristics of Nd^{3+} doped $BaTa_2O_6$ phosphor. Int. J. Appl. Ceram. Technol. 2018;15: 1594–1601. <URL>.

17. Wang X, Zhao H, Li A, Tian K, Brambilla G, Wang P. Near-infrared luminescence and single-mode laser emission from Nd^{3+} doped compound glass and glass microsphere. Front. Mater. Sci. 2019;6:237. <URL>.

18. Prasad RNA, Vijaya N, Babu P, Mohan NK, Praveena R. Optical absorption and NIR photoluminescence of Nd^{3+}-activated strontium phosphate glasses. J. Electron. Mater. 2020;49:6358-6368. <URL>.

19. İlhan M, Ekmekçi MK, Oraltay RG, Başak AS. Structural and near-infrared properties of Nd^{3+} activated Lu_3NbO_7 Phosphor. J. Fluoresc. 2017;27:199–203. <URL>.

20. Ekmekçi MK, İlhan M, Ege A, Ayvacıklı M. Microstructural and radioluminescence characteristics

of Nd^{3+} doped columbite-type $SrNb_2O_6$ phosphor. J. Fluoresc. 2017;27:973–979. <URL>.

21. Ekmekçi MK, Erdem M, Başak AS, İlhan M, Mergen A. Molten salt synthesis and optical properties of Eu^{3+}, Dy^{3+} or Nd^{3+} doped $NiNb_2O_6$ columbite-type phosphors. Ceram. Int. 2015;41:9680–9685. <URL>.

22. Mahamuda Sk, Swapna K, Rao AS, Jayasimhadri M, Sasikala T, Pavani K, Moorthy LR. Spectroscopic properties and luminescence behavior of Nd^{3+} doped zinc alumino bismuth borate glasses. J. Phys. Chem. 2013;74;1308–1315. <URL>.

23. Edwards PR, Martin RW. Cathodoluminescence nano-characterization of semiconductors. Semicond. Sci. Technol. 2011;26:064005. <URL>.

24. Ma DDD, Lee ST, Mueller P, Alvarado SF. Scanning tunneling microscope excited cathodoluminescence from ZnS nanowires**.** Nano Lett. 2006;6:926. <URL>.

25. Dierre B, Yuan XL, Sekiguchi T. Sci. Low-energy cathodoluminescence microscopy for the characterization of nanostructures. Technol. Adv. Mater. 2010;11:043001. <URL>.

26. İlhan M, Güleryüz LF. Cathodoluminescence and photoluminescence of $BaTa_2O_6$:Sm^{3+} phosphor depending on the sintering temperature. Chem. Pap. 2022;76:6963-6974. <URL>.

27. Mitsui T, Yamamoto N, Tadokoro T, Ohta S. Cathodoluminescence image of defects and luminescence centers in ZnS/GaAs(100). J. Appl. Phys. 1996;80:6972. <URL>.

28. İlhan M. Heat capacities and thermodynamic functions of $CdNb_2O_6$ and $CdTa_2O_6$. J. Therm. Anal. Calorim. 2022;147:12383–12389. <URL>.

29. European Coordination Committee of the Radiological, Electromedical and Healthcare IT Industry, COCIR application for new exemption Page 1-12, Blvd A. Reyers 80 1020 Brussels, 2011.

30. Colvin VL, Schlamp MC, Alivisatos AP. Light-emitting diodes made from cadmium selenide nanocrystals and a semiconducting polymer. Nature 1994;370:354–357. <URL>.

31. Chaar LE, Lamont LA, Zein NE. Review of photovoltaic technologies. Renewable Sustainable Energy Rev. 2011;15:2165–75. <URL>.

32. Iorgu AI, Berger D, Alexandrescu L, Vasile BS, Matei C. Synthesis of photoluminescent pure and doped cadmium sulfide by reverse microemulsion method. Chalcogenide Lett. 2013;10:525–531.

33. Willner I, Baron R, Willner B. Integrated nanoparticle–biomolecule systems for biosensing and bioelectronics. Biosens. Bioelectron. 2007;22:1841. <URL>.

34. Choi YJ, Kim YJ, Lee JW, Lee Y, Lim YB, Chung HW. Cyto-/genotoxic effect of CdSe/ZnS quantum dots in human lung adenocarcinoma cells for potential photodynamic UV therapy applications. J. Nanosci. Nanotechnol. 2012;12:2160–2168. <URL>.

35. Su Y, He Y, Lu H, Sai L, Li Q, Li W, Wang L, Shen P, Huang Q, Fan C. The cytotoxicity of cadmium based, aqueous phase – Synthesized, quantum dots and its modulation by surface coating**.** Biomaterials 2009;30:19–25. <URL>.

36. Wong-Ng W, McMurdie HF, Paretzkin B, Kuchinski MA, Dragoo AL. Standard X-Ray Diffraction Powder Patterns of Fourteen Ceramic Phases. Powder Diffr. 1988;3:246-254.

37. Tealdi C, Mozzati MC, Malavasi L, Ciabattoni T, Amantea R, Azzoni CB. Columbite-type $Fe_xMn_{1-x}Nb_2O_6$ solid solution: structural and magnetic characterization. Phys. Chem. Chem. Phys. 2004;6:4056-4061. <URL>.

38. Wachs IE. Infrared spectroscopy of supported metal oxide catalysts. Colloid Surface A. 1995;105:143–149.

39. Ayvacıkli M, Kotan Z, Ekdal E, Karabulut Y, Canimoglu A, Guinea JG, Khatab A, Henini M, Can N. Solid state synthesis of $SrAl_2O_4$:Mn^{2+} co-doped with Nd^{3+} phosphor and its optical properties. J. Lumin. 2013;144:128–132. <URL>.

40. Sontakke AD, Biswas K, Mandal AK, Annapurna K. Concentration quenched luminescence and energy transfer analysis of Nd^{3+} ion doped Ba-Al-metaphosphate laser glasses. Appl. Phys. B 2010;101:235–244. <URL>.

41. MacRae CM, Wilson NC, Torpy A, Davidson CJ. Hyperspectral cathodoluminescence imaging and analysis extending from ultraviolet to near infrared. Microsc. Microanal. 2012;18:1239–1245. <URL>.

42. Lamrani MA, Addou M, Sofiani Z, Sahraoui B, Ebothe J, El Hichou A, Fellahi N, Bernede JC, Dounia R. Cathodoluminescent and nonlinear optical properties of undoped and erbium doped nanostructured ZnO films deposited by spray pyrolysis. Opt. Commun. 2007;277:196–201. <URL>.

43. Hsiao YJ, Fang TH, Ji LW, Chi SS. Surface and photoluminescence characteristics of $CdNb_2O_6$ Nanocrystals. Open Surf. Sci. J. 2009;1:30-33. <URL>.

44. Hsiao YJ, Chang YS, Chen GJ, Chang YH. Synthesis and the luminescent properties of $CdNb_2O_6$ oxides by sol–gel process. J. Alloys Compd. 2009;471:259-262. <URL>.

45. Cherrad H, Addou M, Hssein M, Bahedi K, Jbilou M, Mrigal A, Salmani E, Rouchdi M, Mezred A, Ftouhi H, Diani M, Jouad ME. Theoretical and experimental investigation of structural, electronic and optical properties of neodymium doped ZnO. MATEC Web of Conferences 2020;307:01018. <URL>.

46. El Hichou A, Addou M, Ebothé J, Troyon M. Influence of deposition temperature (Ts), air flow rate (f) and precursors on cathodoluminescence properties of ZnO thin films prepared by spray pyrolysisJ. Lumin. 2005;113:183–190. <URL>.

47. Sittner J, Götze J. Cathodoluminescence (CL) characteristics of quartz from different metamorphic rocks within the Kaoko Belt (Namibia). Minerals 2018:8;190. <URL>.

48. Siegel GH, Marrone MJ. Photoluminescence in as-drawn and irradiated silica optical fibers: an assessment of the role of non-bridging oxygen defect centers. J. Non Cryst. Solids 1981;45:235–247. <URL>.

49. Karl A, Gschneidner Jr, LeRoy E. *Handbook on the Physics and Chemistry of Rare Earths* volume 4 Non-Metallic Compounds – II. 293, 1979.